The Meteoritical Society

Meteoritics & Planetary Science 51, Nr 7, 1353–1369 (2016)
doi: 10.1111/maps.12672

High-pressure phases in shock-induced melt of the unique highly shocked LL6 chondrite Northwest Africa 757

Jinping HU* and Thomas G. SHARP

School of Earth and Space Exploration, Arizona State University, Tempe, Arizona 85287–1404, USA
*Corresponding author. E-mail: jinping.hu@asu.edu

(*Received 06 August 2015; revision accepted 08 May 2016*)

Abstract–Northwest Africa 757 is unique in the LL chondrite group because of its abundant shock-induced melt and high-pressure minerals. Olivine fragments entrained in the melt transform partially and completely into ringwoodite. Plagioclase and Ca-phosphate transform to maskelynite, lingunite, and tuite. Two distinct shock-melt crystallization assemblages were studied by FIB-TEM analysis. The first melt assemblage, which includes majoritic garnet, ringwoodite plus magnetite-magnesiowüstite, crystallized at pressures of 20–25 GPa. The other melt assemblage, which consists of clinopyroxene and wadsleyite, solidified at ~15 GPa, suggesting a second veining event under lower pressure conditions. These shock features are similar to those in S6 L chondrites and indicate that NWA 757 experienced an intense impact event, comparable to the impact event that disrupted the L chondrite parent body at 470 Ma.

INTRODUCTION

Hypervelocity impact has been a fundamental process affecting planets and asteroids through the evolution of the solar system. As a direct product of planetary collisions, shock metamorphism in meteorites provides important material to study the impact histories of their parent bodies. High-pressure minerals are useful indicators of shock pressure, temperature, and pulse duration (Sharp and DeCarli 2006), which are critical for estimating the impact conditions such as the impact velocity, projectile size, and composition (Melosh 1989). Two major issues need to be addressed to better understand the correlation between meteorite shock features and planetary impact conditions. First, the preshock condition of the parent body, even on a microscopic scale, has a strong influence on the resulting shock features. The chemical composition, mineralogy, fracture density, porosity, and grain size of the preshocked sample all determine the way that a shock wave interacts with the material (Melosh 1989). Shock-induced melting on a millimeter scale can cause high local temperatures that facilitate the formation of shock indicators, particularly high-pressure minerals (Langenhorst and Poirier 2000). However the preshock conditions for shocked samples are poorly constrained on a microscopic scale. Second, shock wave propagation is a dynamic process that can produce a variety of shock features in a single shock event. Coexistence of different shock features, forming under varying shock pressure, might suggest different shock levels (Sharp and DeCarli 2006; Xie et al. 2006a). For example, in the highly shocked shergottite Tissint, olivine fragments transformed to ringwoodite are surrounded by shock melt that crystallized olivine and pyroxene (Walton et al. 2014). These features, which, respectively, correspond to pressures >17 GPa and <14 GPa, record pressure evolution during decompression (Walton et al. 2014). To better understand these issues, it is important to investigate a variety of meteorite samples with different preshock conditions and shock histories. However, the availability of highly shocked meteorites is limited to several groups. The large population of ordinary chondrites contains many highly shocked samples, but primarily in the L group (Stöffler et al. 1991). On the contrary, there are very few highly shocked samples in the LL chondrite group to constrain the impact history of the LL parent body.

Many highly shocked L chondrites have been investigated in detail (Chen et al. 1996; Sharp et al. 1997; Tomioka and Fujino 1997; Ohtani et al. 2004; Xie

et al. 2006a, 2006b; Ferroir et al. 2008; Miyahara et al. 2009; Ozawa et al. 2009; Tschauner et al. 2014). These studies have provided fundamental knowledge about the nature of shock metamorphism in meteorites. The high-pressure assemblages in L chondrites commonly include ringwoodite, wadsleyite, garnet, akimotoite, vitrified bridgmanite, and magnesiowüstite plus magnetite. Thermodynamic properties of these minerals indicate a shock pressure up to ~25 GPa (Tschauner et al. 2014). Moreover, the shock-pulse durations in L chondrites have been estimated, by shock-melt quench history (Sharp et al. 2015), high-pressure transformation kinetics (Chen et al. 2004; Miyahara et al. 2010), and element diffusion (Beck et al. 2005), to be hundreds of milliseconds to several seconds. The shock pressure (P)-temperature (T)-time (t) history extracted from meteorites reflects the impact velocity and projectile size on the meteorite parent body. Ohtani et al. (2004) and DeCarli et al. (2012) used the estimates of shock duration to constrain the size of the impactor on the L parent body, employing a planar impact approximation, and hydrocode simulations, respectively. These two studies both concluded that the L chondrite parent body was impacted by a projectile >10 km in diameter. Noble gas age dating of many shocked L chondrites record a large impact at ~470 Ma (Turner 1969; McConville et al. 1988; Bogard 1995; Korochantseva et al. 2007; Weirich et al. 2012), which is consistent with evidence for a long shock duration.

Although the L chondrites provide useful material for understanding shock effects, their origin in a relatively young catastrophic impact event may not be representative of asteroid impact histories. It is essential to investigate shock metamorphism in other types of chondrites to learn more about broader asteroid impact histories. Unlike the shocked L chondrites, H chondrites record diverse impact ages older than 3.5 Ga and younger than 1.0 Ga (Bogard 1995; Swindle et al. 2014). The older ages record early accretion (>4400 Ma) and late heavy bombardment (3500–4100 Ma). The diverse ages younger than 1000 Ma suggest either several impact events or partial resetting by at least one young impact at ~280 Ma (Swindle et al. 2014). The same high-pressure assemblages that occur in highly shocked L chondrites have been reported for H chondrites but in fewer samples (Kimura et al. 2000, 2003). Distinct from L and H ordinary chondrites, shock effects in LL chondrites have not been extensively observed or studied. Except for those in NWA 757, jadeite, reported in LL5 chondrite Y-8410 (Kimura et al. 2001) and in the Chelyabinsk LL5 chondrite (Ozawa et al. 2014), is the only high-pressure mineral reported in LL chondrites. Both studies interpret a lower shock pressure and a shorter shock duration than those of highly shocked L chondrites and they infer a less intense impact event on the LL source body. The paucity of highly shocked LL chondrites suggests that either the LL-chondrite parent body did not experience intense asteroid impacts, or highly shocked materials from the LL parent body have not been stochastically captured by the Earth. NWA 757 is a unique high-pressure mineral-bearing LL chondrite that provides new information about impacts on its parent body.

Bischoff (2002) reported olivine transformation to ringwoodite in LL6 chondrite NWA 757. It is the only report of high-pressure minerals in an LL chondrite. In this study, we investigated the high-pressure minerals in NWA 757, formed by solid-state transformation and by shock-melt crystallization, to determine shock conditions. The P-T-t history is compared with those from highly shocked L chondrites. We use the shock features in NWA 757 to discuss possible impact conditions and history of LL chondrite parent bodies.

SAMPLE AND METHODS

NWA 757 is an ordinary chondrite that was purchased in Rissani, Morocco and classified as type LL6 with shock stage S4 and weathering grade W2 (Bischoff 2002). The thin section PL01135 in this study was provided by the Institut für Planetologie/ICEM. The petrologic microscope was used to document melt-vein thickness and internal textures and to identify mineral fragments transformed to high-pressure minerals such as ringwoodite. Transformed fragments were confirmed by Raman spectroscopy, using a 532 nm unpolarized laser with power of 1.3–6.5 mW. The laser is focused by a 50× objective lens with 1 cm focal length. The laser spot size on the sample is 0.5 μm. Spectra were collected from 100 to 2200 cm^{-1} for 20–60 s. Detailed shock vein textures were investigated by scanning electron microscopy (SEM) using an FEI XL30 with a field-emission gun and energy dispersive X-ray spectroscopy (EDS). The typical SEM operating conditions included an accelerating voltage of 20 kV, a working distance of 11–5 mm, and a probe current of 3–10 nA. EDS with an EDAX SiLi EDS X-ray detector was employed to acquire chemical compositions of mineral phases of interest. The setup used a process time of 4–10 μs for count rates greater than 1000 counts per second and up to 30% dead time. Absorption and fluorescence effects were corrected with a ZAF model. Raman spectroscopy and SEM were done in the LeRoy-Eyring Center for Solid State Science (LE-CSSS) at Arizona State University.

Shock-vein mineralogy and microstructures were investigated with transmission electron microscopy (TEM) using an FEI CM200-FEG in the LE-CSSS.

TEM samples were prepared by focused ion beam (FIB) lift-out techniques with an FEI Nova200 NanoLab. The CM200 was operated at 200 kV. Bright-field TEM imaging was used to investigate melt-vein textures, mineral intergrowths, and defects. Mineral phases were identified by selected-area electron diffraction (SAED), accompanied by EDS chemical analysis using an EDAX SiLi EDS X-ray detector. Quantitative EDS data processing was performed with an Emispec Vision system.

Synchrotron micro-X-ray diffraction was performed on the thin section at GSE-CARS at the Advanced Photon Source, Argonne National Lab, using the sector 13BM-D bending magnet, which has a 5×12 μm focused X-ray beam. An X-ray energy of 30 keV ($\lambda = 0.4137$Å) was used for the analysis. Refinement was performed with GSAS software (Larsen and Von Dreele 1994; Toby 2001) with initial peak shape defined by the 13BM-D instrumental parameter file. Cell parameters, intensity scaling, and peak shape were refined in the software.

RESULTS

Petrography

The host rock of NWA 757 consists of olivine, enstatite, diopside, plagioclase plus minor Fe-Ni alloy, troilite, and chromite. The host rock is mostly recrystallized overall. However, several chondrules can still be delineated in the thin section and they show metamorphosed barred olivine or porphyritic olivine textures. Plagioclase grains are commonly larger than 100 μm. Some poorly recrystallized plagioclase aggregates with grain size below 10 μm (Fig. S1) suggest heterogeneous thermal metamorphism. Bischoff (2002) analyzed compositions of olivine and low-Ca pyroxene as 28.1 ± 0.7 mole% fayalite and 23.4 ± 0.8 mole% ferrosilite. The host-rock olivine and pyroxene grains, up to a few hundred microns in size, have abundant irregular and planar fractures. Some olivine grains (less than 10%) show strong mosaicism or undulatory extinction (Fig. S1) while most of the grains (more than 50%) have weak undulatory or sharp extinction under cross-polarized light. Maskelynite coexists with crystalline plagioclase throughout the thin section (Fig. S1). Based on the fact that more than 25% of the feldspar is crystalline plagioclase (Stöffler et al. 1991), Bischoff (2002) classified the shock stage as S4. However, the high-pressure minerals associated with the shock melt indicate shock stage S6. The S6 features and high-pressure phases are characterized in the next section. Secondary oxide veins and calcium-rich veins are inferred to be a result of weathering. These secondary veins cut through the shock-induced melt veins, suggesting a late epigenetic origin. Dark orange staining of the host rock through the thin section (Fig. 1a) is mostly from terrestrial oxidation. Most iron-sulfide grains are fresh, which is consistent with weathering grade W2.

The shock-induced melt in NWA 757 occurs as a complex network of shock veins and melt pockets (Fig. 1a). The shock vein widths vary from 1 mm to several microns. The shock melt consists of quenched immiscible silicate plus metal/sulfide liquids. Finely disseminated metal/sulfide droplets (Fig. 1e) and aggregates make the shock melt opaque in thin section (Fig. 1d). The host-rock fragments included in the shock veins and melt pockets range from 10 to 500 μm in size. Abundant high-pressure minerals in the shock melt indicate a shock stage of S6. The apparent inconsistency between S6 shock melt and the S4 host rock is discussed in following sections.

Solid-State Transformation

In the shock melt, the host-rock fragments of olivine-composition are completely or partially transformed to polycrystalline ringwoodite aggregates. The ringwoodite varies in color from dark blue to light blue, light green, and colorless in plane-polarized light. Continuous variation in color is visible in large individual fragments (Figs. 1b, 1c, and 1d). Raman spectral characteristics of ringwoodite vary with color. All the ringwoodite spectra have the broad 230 cm^{-1} peak with a strong background from fluorescence (Fig. 2). The relative intensity of the fluorescent background is lower in colorless ringwoodite. Spectra of blue and green ringwoodite show diagnostic 799 and 842 cm^{-1} peaks (Fig. 2) while these peaks are weaker in colorless ringwoodite. Most ringwoodite fragments are uniform with no distinguishable reaction textures or chemical heterogeneity visible in back-scattered electron (BSE) images, indicating that most olivine fragments within the shock vein were completely transformed to fine-grained ringwoodite aggregates. The homogeneous ringwoodite aggregates in BSE images suggest that the reaction was interface controlled, with no iron segregation between ringwoodite and olivine during the transformation (Kerschhofer et al. 1998). However, several unusual fragments have the two olivine Raman peaks, at 824 cm^{-1} and 853 cm^{-1}, combined with the broad ringwoodite peak at 232 cm^{-1} (Fig. S2). Inferred from the contrast variation in the BSE images and Raman spectra, these are partially transformed olivine fragments with lamellar ringwoodite intergrowths (Fig. 3a). These ringwoodite lamellae have variable orientations and thicknesses. Nano-scale lamellae of two

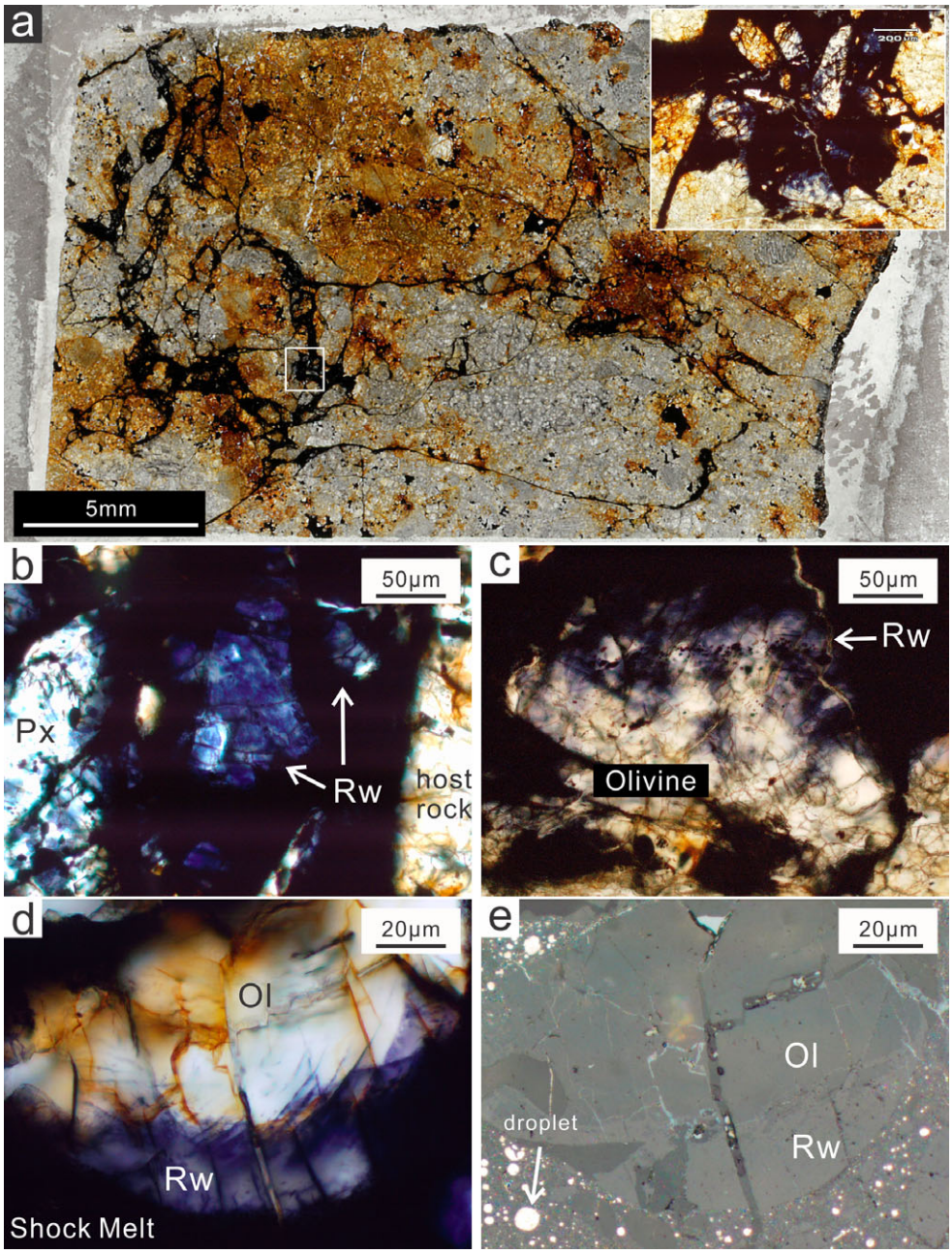

Fig. 1. Optical images of NWA 757 thin section PL01135. Rw = ringwoodite, Px = pyroxene, Ol = olivine. a) Transmitted-light image of the NWA 757 thin section. The orange color is from terrestrial oxidation. The opaque veins and pockets are shock melt. A plane-polarized light (PPL) microscopy image of a 1-mm-thick melt pocket (white box) is enlarged at the top of image (a). Translucent grains in the melt pocket are host-rock fragments. b) PPL image of dark blue to light blue ringwoodite fragments in shock melt. The bright clast on the left side of the image is untransformed pyroxene. c) Colorless olivine clast that is partially transformed to blue ringwoodite along the clast margin with the shock melt. d) Another example of colorless olivine partially transformed into blue ringwoodite. e) Reflected light image of the same olivine grain shown in (d), showing ringwoodite with higher reflectivity than olivine and high-reflectivity metal-sulfide droplets in the shock melt.

predominant directions cross with an angle of ~60°/120°. Thicker lamellae (1 μm) are less regularly oriented. These lamellar features are similar to those reported in Sixiangkou and Y-791384 L6 chondrites (Chen et al. 2004; Miyahara et al. 2010). Future work is needed to confirm the crystallographic and interface relationships between olivine and ringwoodite. In these partially transformed fragments, the ringwoodite is most abundant at the edges in contact with the shock melt (Figs. 1c and 1d).

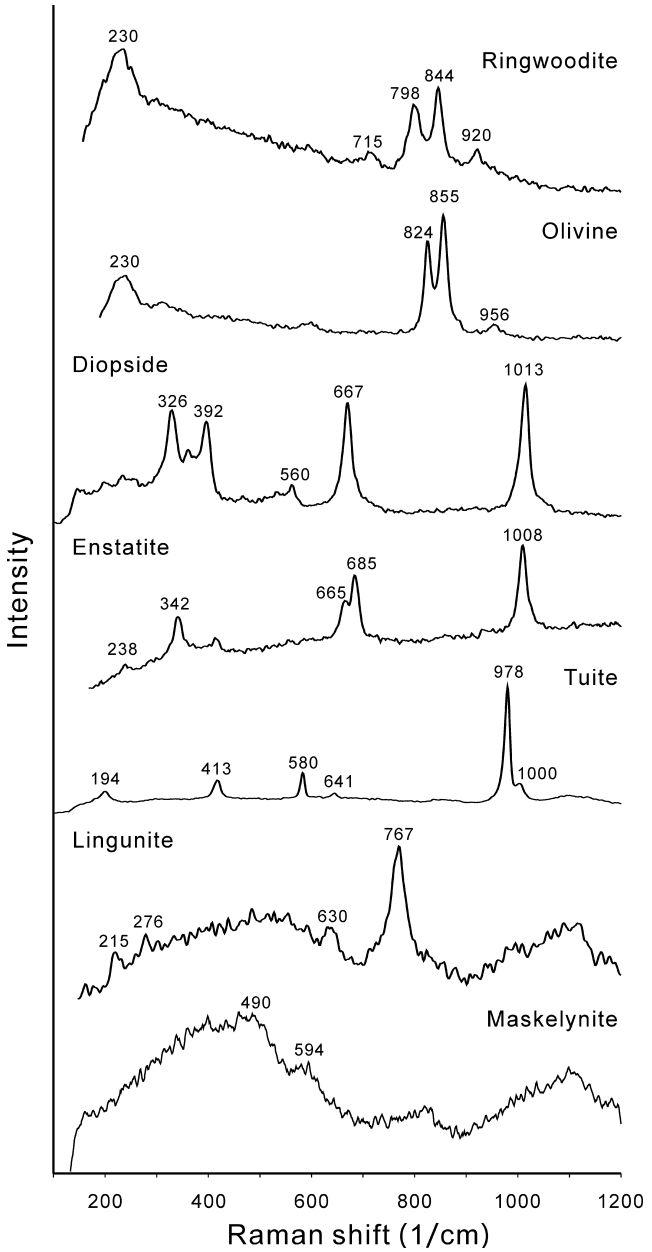

Fig. 2. Raman spectra of mineral fragments entrained in the shock melt. Intensity is given in arbitrary units for comparison of multiple spectra. Major peak positions for each phase are labeled in wave number (cm^{-1}) units.

In the shock melt, both low-Ca and high-Ca pyroxene fragments are common. Raman spectroscopy shows that they are clinoenstatite and diopside (Fig. 2). No evidence for pyroxene transformation to high-pressure polymorphs has been found in this sample. The pyroxene fragments in melt veins are homogeneous in both PPL and BSE images. They commonly have sharp extinction and a low density of irregular fractures (Fig. 1b).

Ca-phosphate in the shock melt occurs as small accessory clasts. Raman spectra indicate that they are tuite (high-pressure γ-$Ca_3(PO_4)_2$, Fig. 2). The diagnostic peaks match well with tuite from shocked chondrites and γ-$Ca_3(PO_4)_2$ synthesized by high-pressure experiments (Xie et al. 2013). The tuite clasts are commonly smaller than 10 μm in size and homogeneous in BSE images.

Polymorphic phases of feldspar include shocked plagioclase, maskelynite, normal glass, and lingunite. Aside from shock-melt veins, the feldspar is either crystalline plagioclase or maskelynite (diaplectic glass). Locally maskelynite and plagioclase coexist in one grain (Fig. S1). The Raman spectrum from maskelynite shows broad peaks at 490 and 594 cm^{-1} (Fig. 2). The maskelynite is optically isotropic and surrounded by radial fractures that indicate a large expansion during decompression. The feldspar near the melt veins has optical isotropy, flow features, and silicate fragment inclusions (Fig. 4a). These grains are inferred to be normal glass quenched from feldspar melt. Some plagioclase fragments within shock veins have Raman spectra (Fig. 2) consistent with lingunite, the high-pressure polymorph of plagioclase with the hollandite structure. Lingunite fragments occur exclusively in shock melt and coexist with ringwoodite and enstatite clasts, entrained in one of the thickest melt pockets (Fig. 4b).

Shock-Melt Crystallization

The melt-vein matrix consists of silicate plus oxide minerals and metal-alloy plus iron-sulfide droplets. As in other shocked chondrites (Chen et al. 1996), this mixture is inferred to represent immiscible silicate and metal-sulfide liquids that are rapidly quenched during shock to preserve high-pressure phases. In this sample, there are two distinct shock-vein quench textures and assemblages (Table 1), Type HP (higher pressure) and Type LP (lower pressure), which are distinguishable by XRD, SEM, and TEM observations.

Type HP Quenched Melt

The Type HP melt matrix occurs mostly in the thick melt veins and pockets. This matrix consists of equant-subhedral silicate crystals and two interstitial phases with lighter BSE contrast as well as disseminated metal-sulfide droplets or veins (Fig. 3b). Synchrotron X-ray diffraction patterns indicate the occurrence of garnets, troilite, and metallic iron (Fig. 5). Refinement of the XRD patterns gives the garnet space group *Ia*-3*d* and unit cell parameter 11.53Å. The space group and unit cell parameters of troilite are *P*-62*c*, a = 5.98 Å, and c = 11.70 Å. TEM SAED patterns show that the

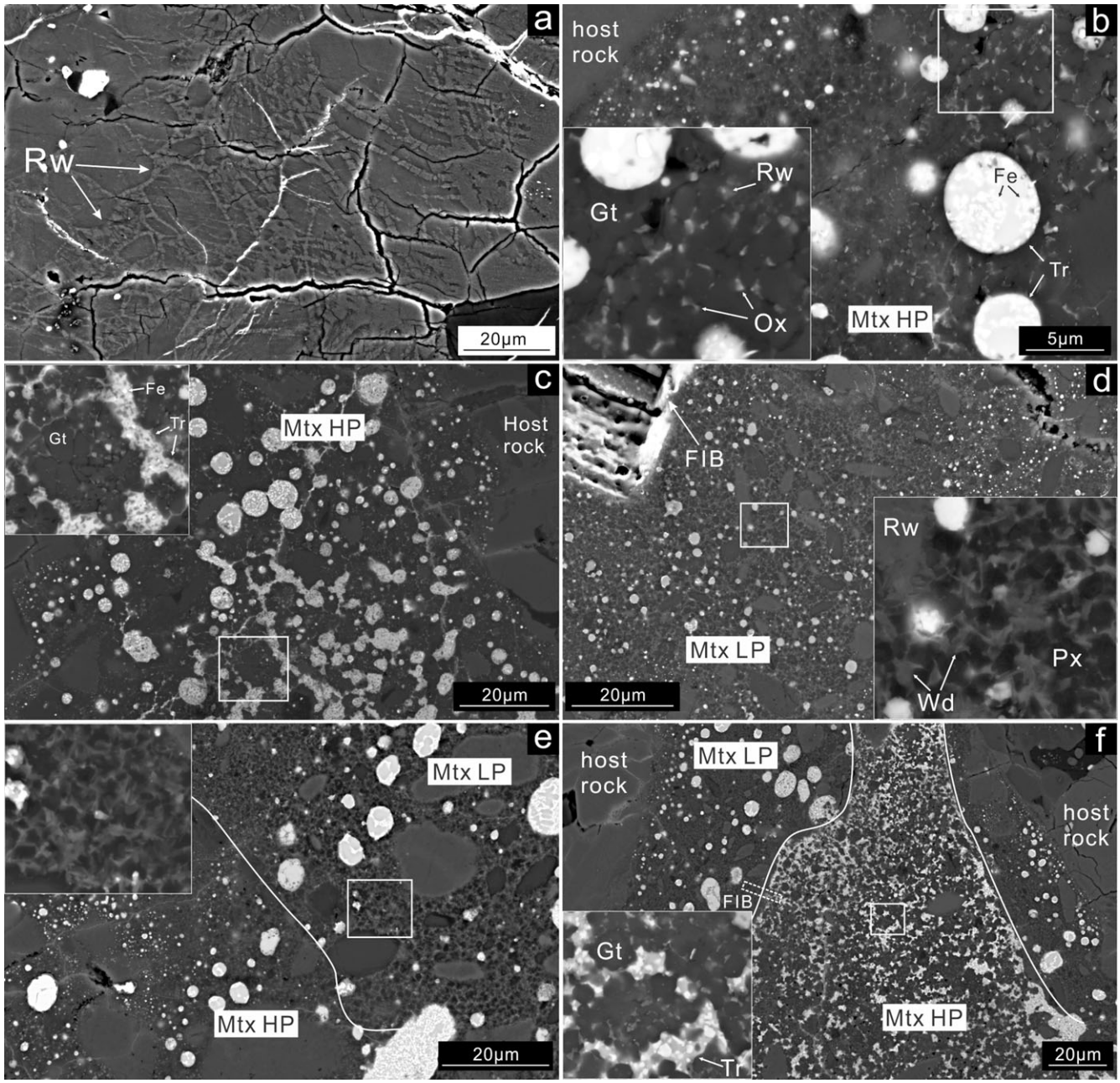

Fig. 3. BSE images of high-pressure mineral occurrences in and adjacent to shock veins. In each figure the white box outlines the area shown in the high magnification inset image. Rw = ringwoodite, Wd = wadsleyite, Gt = garnet, Px = clinopyroxene, Ox = magnesiowüstite-magnetite, Tr = troilite, Fe = nickel-iron alloy, Mtx HP = Type HP quenched melt, Mtx LP = Type LP quenched melt. a) Lamellar ringwoodite (lighter contrast) in a partially transformed olivine clast. Two predominant orientations of the lamellae intersect at ~120°. b) Type HP melt matrix, showing quenched silicate and sulfide liquids. The predominant dark gray phase is garnet. Interstitial bright-gray phases are ringwoodite/wadsleyite and magnesiowüstite-magnetite. Black regions are residual glass, altered glass, or voids. The bright round objects are quenched metal-sulfide droplets consisting of troilite (gray) and Fe-Ni metal (white). The crystal size in the vein decreases toward the vein edge. c) Type HP melt matrix with the same silicate texture as (b), but with the sulfide texture varying from round droplets to irregular veins and droplets in the interior. The dark gray phases in the sulfide veins are silicate inclusions. d) A 200-μm-thick Type LP melt vein. The matrix consists of granular clinopyroxene (dark gray) and elongated wadsleyite (light gray). The grain size of silicates grades from ~500 nm in the vein interior to finer at the vein edge. The round bright droplets are predominantly sulfide. A FIB-TEM section was taken from the milled pit in the upper left of the image. e) Gradational contact between HP and LP melt textures. Both are fine-grained and contain round droplets with variable sulfide-metal mixtures and textures. f) Sulfide-rich Type HP matrix in contact with sulfide poor Type LP matrix. The sharp boundary is defined by a transition in the sulfide texture from round droplets in Mtx LP to irregularly disseminated sulfide in Mtx HP. A FIB section was taken from the interface (dashed-line box).

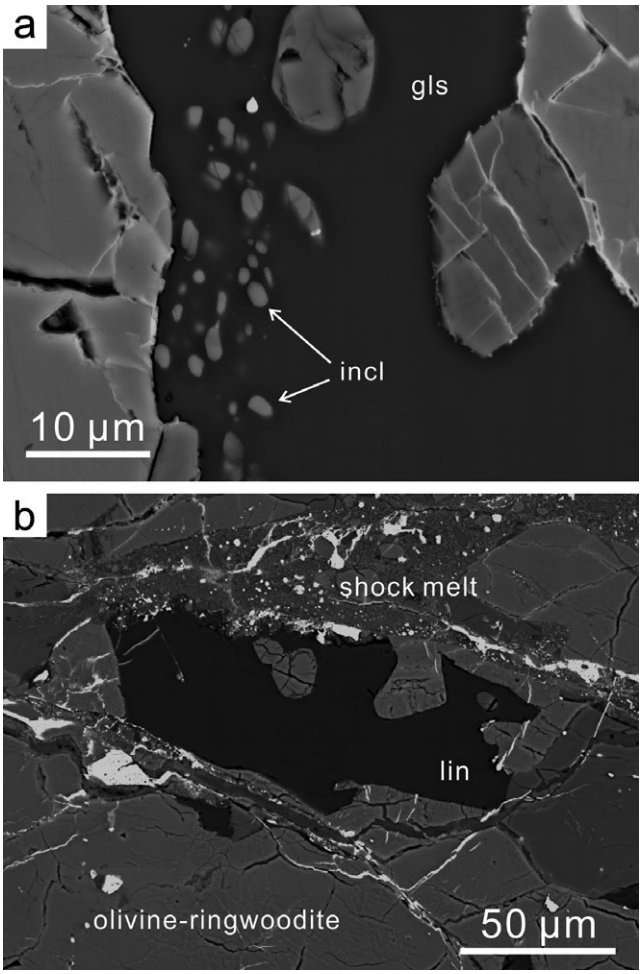

Fig. 4. SEM BSE images of normal feldspar glass (gls) and lingunite (lin). a) The dark-contrast feldspar glass shows flow features and entrains silicate inclusions (incl). The inclusions have curved edges and flow features. b) The dark-contrast lingunite grain is in contact with shock melt and partially transformed olivine. This grain shows flow features and is homogeneous.

equant silicates in BSE images are garnet and the two bright phases in between are ringwoodite and magnetite. EDS analysis of the garnet ($Na_{0.15}Ca_{0.23}Fe_{0.96}Cr_{0.02}Mg_{2.4}Al_{0.36}Si_{0.88}Si_3O_{12}$) indicates a large majorite component (majoritic garnet) with 0.88 pfu excess silicon in the octahedral site (Table 2). Previous studies described the garnet crystallized from shock melt in chondrites as majorite-pyrope solid solution (Chen et al. 1996; Miyahara et al. 2010). However, our and previous data commonly indicate the garnet has a grossular component as well as sodium. The sodium endmember $MgNa_2Si_5O_{12}$ has not been named (Grew et al. 2013). Therefore we use majoritic garnet to describe the garnet with a high majorite fraction and other components in addition to pyrope.

Table 1. Summary of the differences between Type HP and Type LP melt matrix.

Melt matrix	Type HP	Type LP
Mineral	Garnet, ringwoodite, wadsleyite, magnesiowüstite/ magnetite	Clinopyroxene, wadsleyite
Grain size	Fine (100 nm) to coarse (3 μm)	Fine (100 nm to 1 μm)
Distribution	In middle-sized melt pockets and veins (100–500 μm)	In melt veins of all thickness
Sulfide	Abundant, round droplets, and irregular veinlets	Depleted, only round droplets

The ringwoodite (*Fd*-3 *m*) crystals are anhedral and full of dislocations and localized strain (Fig. 6b). Although magnesiowüstite is the oxide phase expected from chondritic melt crystallization at high pressure, magnetite occurs in the Type HP assemblage. Previous studies have interpreted topotaxially intergrown magnetite and magnesiowüstite, with the crystallographic relationship $<110>_{Mw} \| < 110>_{Mag}$, to be a result of exsolution from a ferric-iron bearing magnesiowüstite (Chen et al. 1996; Xie et al. 2006a). The magnetite-wüstite in NWA 757 shock melt occurs either as triangular interstitial crystals between garnets (Fig. 6a), or in association with wadsleyite (Fig. 6c). The contrast in the images indicates local strain that is likely associated with intergrown magnetite and wüstite. Wadsleyite (*Imma*) occurs locally and in association with magnetite. SADP shows the wadsleyite-magnetite assemblage has an orientation relationship such that $<110>_{Mag} \| < 212>_{Wads}$. The overlapping diffraction spots in this zone axis pattern indicate parallel planes $\{111\}_{Mag} \| \{101\}_{Wads}$ and $\{004\}_{Mag} \| \{240\}_{Wads}$ (Fig. 6c). This crystallographic relationship is the same as the wadsleyite-magnetite association from the shock melt in L6 chondrite Roosevelt County 106 (Sharp et al. 2015). The crystal size in the matrix is typically 1 μm for the garnet, 300 nm for the ringwoodite, and 100 nm for the magnetite. The silicate minerals are all finer than 100 nm at the edge of the vein (Fig. 3b).

Polycrystalline weathering products (Fig. 6f) commonly occur next to the iron-oxide grains and are inferred to result from terrestrial weathering of residual silicate glass left by fractional crystallization of garnet and magnesiowüstite. The texture of the weathering phases is similar to the clay minerals from weathered glass in L6 chondrite RC 106 (Sharp et al. 2015). The very low contrast materials between garnet crystals in the BSE images correspond to the residual glass or clays

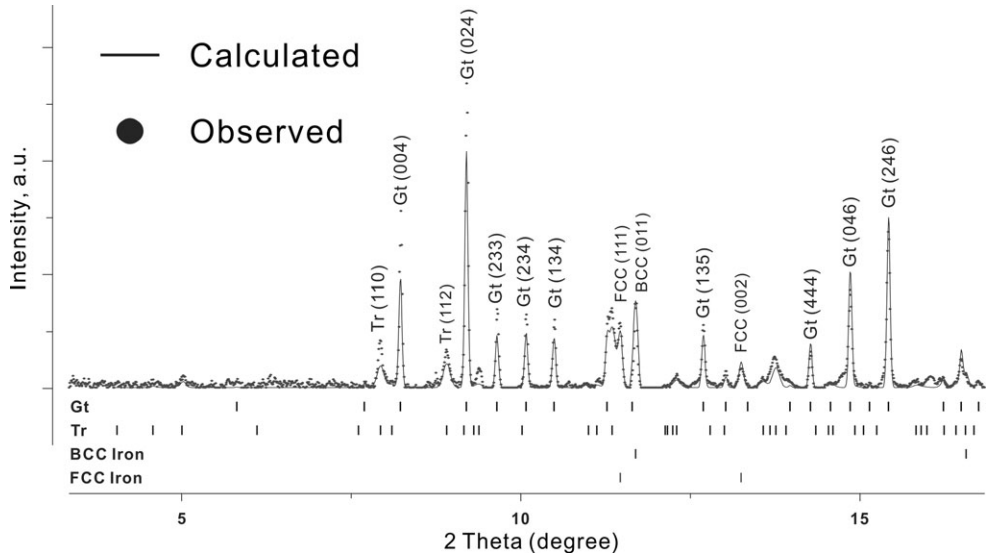

Fig. 5. Synchrotron micro-XRD pattern of Type HP matrix (dots) and calculated XRD pattern (solid line) for a mixture of garnet, troilite, body-centered cubic iron alloy, and face-centered cubic iron alloy. A systematic disagreement occurs between the data and the calculation. The calculated intensity is lower at low diffraction angle.

Table 2. Compositions and formulae of garnet and pyroxene in the shock melt.

	gnt	px
Na_2O	1.05	2.18
MgO	22.19	22.30
Al_2O_3	4.20	6.12
SiO_2	53.38	56.97
CaO	3.00	3.17
Cr_2O_3	0.32	n.d.
FeO	15.86	9.26
Formula	gnt	Px
Na	0.15	0.15
Mg	2.40	1.16
Al	0.36	0.25
Si	3.88	2.00
Ca	0.23	0.12
Cr	0.02	
Fe	0.96	0.27
Oxygen	12.00	6.00

The compositions, in oxide weight percentage, are normalized to 100%. The calculated formulae of garnet (gnt) from Type HP melt and pyroxene (px) from Type LP melt are normalized to 12 and 6 oxygens, respectively.

(Fig. 3b). The soft clay may also be polished out in sample preparation, leaving dark-contrast voids in BSE images.

The abundance and morphology of metal-sulfide varies throughout the Type HP matrix. In a melt pocket of 100 μm width, the sulfide occurs as well-defined spheroidal droplets up to 10 μm in diameter near the pocket edge (Fig. 3c). The droplets are mixtures of troilite and round particles of Fe-Ni metal. Synchrotron XRD indicates the coexistence of both face-centered cubic and body-centered cubic iron alloy (Fig. 5). For the melt pocket interior, the quenched sulfide melt forms a network of veins (Fig. 3c). Many silicate inclusions are entrained in the sulfide veins. The metal particles are much less common in the sulfide veins than in the droplets, indicating a heterogeneous composition of the metal-sulfide melt (Figs. 3b and 3c). In another melt pocket, the quenched sulfide does not preserve the shape of immiscible droplets (Fig. 3f). Anhedral sulfide, enriched in iron-nickel particles, fills interstices between the garnet crystals (Fig. 3f).

Type LP Quenched Melt

The other type of quenched melt matrix is distinctively different in texture and mineralogy from Type HP. It occurs in both thin and thick melt veins. Two fine-grained silicate phases with round sulfide droplets are predominant in matrix Type LP (Fig. 3d). TEM SAED indicates the dark BSE contrast phase is clinopyroxene ($P2_1/c$). EDS analysis indicates the pyroxene is sodium-bearing pigeonite (Table 2). The elongated bright contrast phases are wadsleyite and trace ringwoodite. Common <010> stacking faults occur in the wadsleyite and their resulting stacking disorder is indicated by the streaks along b* in the diffraction pattern (Fig. 6e). The silicates are typically 200–500 nm in size at the melt vein interior, grading into finer-grained crystals at the melt-vein edge. Sulfide droplets in the Type LP matrix are consistently round and vary in size from submicron to 10 μm.

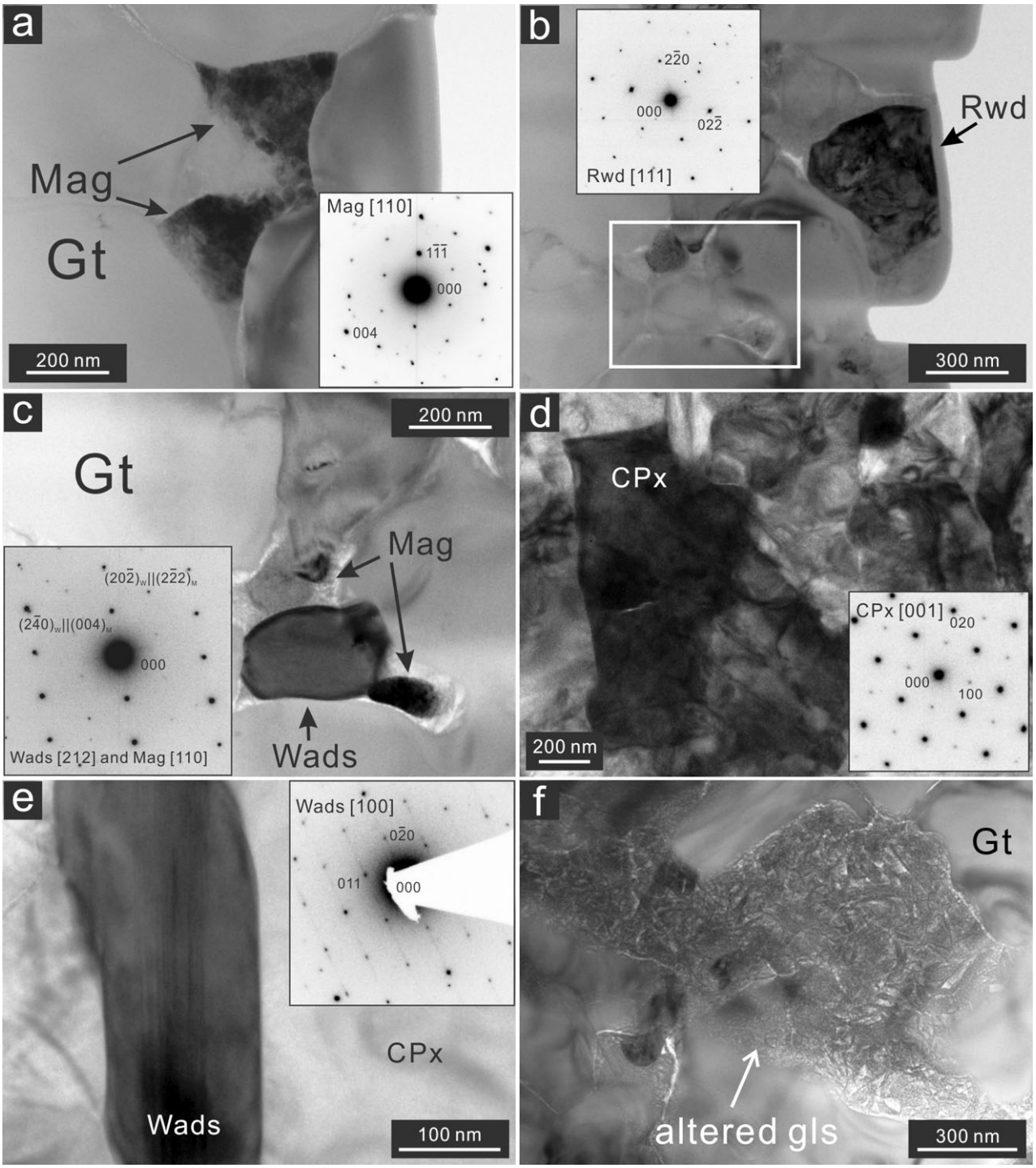

Fig. 6. TEM micrographs of FIB sections from the crystallized shock melt. Mag = magnetite, Rwd = ringwoodite, Gt = garnet, Wads = wadsleyite, CPx = clinopyroxene, Tr = troilite. Image (a), (b), and (c) are from the Type HP matrix and image (d) and (e) are from Type LP matrix. Electron diffraction patterns of the minerals are shown as inset images. a) Magnetite (dark contrast) occurs in the interstices between majorite garnet crystals. The mottled internal texture in the magnetite indicates local strain contrast, which may be from intergrown wüstite. b) Fine ringwoodite crystal (dark contrast) between majorite garnets. The strain contrast in ringwoodite results from dislocations. The white box outlines the area show in (c). c) Association of magnetite and wadsleyite with an orientation relationship with $<212>_{wads||}<110>_{mag}$. The other magnetite crystal (light contrast) above the wadsleyite does not have an orientation relationship. d) Type LP matrix contains predominantly clinoenstatite. e) An elongated wadsleyite crystal shows a vertical set of stacking faults. Streaks along 010* in the electron diffraction pattern indicate stacking disorder from stacking faults on (010). f) Weathering products (altered gls) from the residual glass left by fractional crystallization.

Table 3. Bulk compositions of Type HP and Type LP quenched melt and atomic ratio compared to peridotite and CV3 chondrite.

	Matrix HP (6)	2σ	Matrix LP (7)	2σ	Atomic ratio	Matrix HP	Matrix LP	KLB-1	Allende
Na_2O	1.16	0.15	2.20	0.49	Na/Si	0.045	0.089	0.013	0.020
MgO	26.16	0.38	25.95	0.66	Mg/Si	0.780	0.812	1.329	1.151
Al_2O_3	3.63	0.18	3.97	0.33	Al/Si	0.086	0.098	0.094	0.123
SiO_2	49.99	0.60	47.65	0.87	Ca/Si	0.053	0.059	0.073	0.067
P_2O_5	0.20	0.27	n.d.						
CaO	2.48	0.32	2.64	0.20					
FeO	16.38	0.52	17.59	0.26					

The bulk compositions, in oxide weight percentage, are normalized to 100%. The number of analyses is shown in the brackets. The compositions of peridotite KLB-1 and CV3 chondrite Allende are from Zhang and Herzberg (1994) and Agee et al. (1995), respectively.

We measured the bulk compositions of Type HP and LP matrices by SEM-EDS. Each analysis is a raster on at least 5×5 μm^2 area (Table 3), targeted to exclude the sulfide droplets from these analyses. This is confirmed by the lack of detectable sulfur. However, a small amount of phosphate is detected in the Type HP matrix analysis. The two matrix types are not significantly different in most major elements. The Type LP matrix is slightly more enriched in iron and depleted in silicon. The major difference is that the concentration of sodium in Type LP is about twice of that in Type HP.

The two matrix types occur mostly in separate melt veins but they are in contact locally in several melt pockets (Figs. 3e and 3f). Their contact boundaries are not generally well defined (Fig. 3e). Both matrices are relatively fine grained on the boundary. Sulfide droplets commonly have similar sizes and textures through the two melts (Fig. 3e). The melt pocket in Fig. 3f shows a better-defined boundary between the two matrices. The different shapes and abundance of sulfide make the matrix type transition appear sharp. The Type LP matrix clearly becomes fine grained toward the host rock. In contrast, the Type HP matrix has less grain-size variation. Figure 3f shows what appears to be Type HP matrix crosscutting the Type LP matrix. However, our focused ion beam section from this area shows a gradual transition of the silicate assemblage between the two types. The lack of consistent sharp boundaries and clear crosscutting relationships (Fig. 3e) makes the timing of the two vein-forming events unclear.

DISCUSSION

Melt Crystallization Pressure and Shock Pressure

The shock-melt crystallization assemblage provides constraints on the shock pressure conditions during the quench of the shock melt. The high-pressure assemblages in chondrite shock veins are generally consistent with the liquidus phase relations derived from static high-pressure experiments, such as those in Sixiangkou, Tenham, and Y-791384 L6 chondrites (Chen et al. 1996; Ohtani et al. 2004; Xie et al. 2006a). We do not imply that the rapid quench of a shock-induced melt represents thermodynamic or chemical equilibrium. However the crystallization assemblages can provide useful and consistent estimates of *P-T-t* histories during shock. The chondritic shock melts in small veins quench quickly after their formation and record the pressure-temperature conditions during shock (Langenhorst and Poirier 2000; Sharp and DeCarli 2006). Because shock veins quench primarily by conduction of heat into the surrounding solid host rock, the quench time is dependent on the volume and initial temperature of the melt and the temperature of the host rock. The edge of a melt vein in contact with the host rock quenches faster than the vein center. This is advantageous because thin veins and vein edges can quench rapidly enough to record the peak shock pressure by the crystallization assemblage. In contrast, thick veins and larger melt pockets quench more slowly and may record lower pressures if the crystallization occurs during decompression (Xie et al. 2006a; Miyahara et al. 2011a, 2011b). For a thick vein with a constant high-pressure assemblage, it can be inferred that the crystallization pressure and the corresponding shock pressure remained high throughout the duration of the shock-vein quench.

Minerals such as ringwoodite, lingunite, and tuite, which form by solid-state transformation of minerals entrained in shock veins, can also constrain shock pressure estimates. However, high-pressure transformations, such as olivine to ringwoodite, can occur metastably well below the wadsleyite-ringwoodite equilibrium phase boundary that defines the stability field of ringwoodite (Sharp and DeCarli 2006; Walton et al. 2014). In contrast, pyroxene fragments are commonly preserved metastably at high pressure because of the slow rates of transformation (Hogrefe

et al. 1994). Thus, temperature and reaction kinetics are as important as pressure in controlling the transformation products. In some large olivine fragments (Figs. 1c and 1d), the ringwoodite transformation occurs exclusively along the boundary with shock melt, indicating that very high temperatures are required for the transformation. Therefore, solid-state transformation of silicates in and adjacent to shock melt generally provides only loose constraints on shock pressure.

The apparent discrepancy of shock stages between the shock melt veins (S6) and the host rock (<S5) is unlikely a result of local pressure excursions because the pressure variations only occur during shock loading and rapidly ring out to an equilibrium shock pressure. The crystallization of shock melt occurs after shock-pressure equilibration (Sharp and DeCarli 2006). We suggest that in samples that have S6 melt veins in a matrix of lower shock stage indicators, the classification should be S6.

The two types of melt matrix in the sample indicate different crystallization pressures. Matrix Type HP consists of majoritic garnet, ringwoodite, magnetite, clay plus metal-sulfide. The magnetite and clay are formed by postshock exsolution and alteration of magnesiowüstite and weathering of residual-melt glass (Chen et al. 1996). Based on the liquidus phase diagram of Allende CV3 chondrite (Agee et al. 1995; Asahara et al. 2004), the assemblage is consistent with a pressure of ~20–25 GPa (Fig. 7). Unlike the garnet plus magnesiowüstite assemblage of S6 L6 chondrite Sixiangkou (Chen et al. 1996), NWA 757 matrix Type HP also contains ringwoodite, which suggests a somewhat lower crystallization pressure than that of Sixiangkou. The interstitial occurrence of ringwoodite and oxide between garnets is consistent with garnet being the liquidus phase.

The mineral assemblage in Type LP matrix complicates the interpretation of crystallization pressure. This assemblage consists of clinopyroxene, wadsleyite, minor ringwoodite plus metal-sulfide droplets. None of the phase diagrams from either chondrite, peridotite, or basalt indicates a liquidus assemblage of clinopyroxene plus wadsleyite that excludes garnet and olivine (Zhang and Herzberg 1994; Agee et al. 1995; Hirose et al. 1999). Olivine and garnet are the liquidus phases at pressures below ~14 GPa and between 14 and 22 GPa, respectively (Fig. 7). The slight difference in composition of Type LP matrix cannot account for the lack of garnet as a liquidus phase. The clinopyroxene and wadsleyite in the Type LP matrix are likely subsolidus phases that crystallized from a supercooled melt. Both minerals are subhedral and nanocrystalline (~200 nm) (Figs. 6d and 6e). Supercooling of the Type LP melt to below the solidus could result in metastable

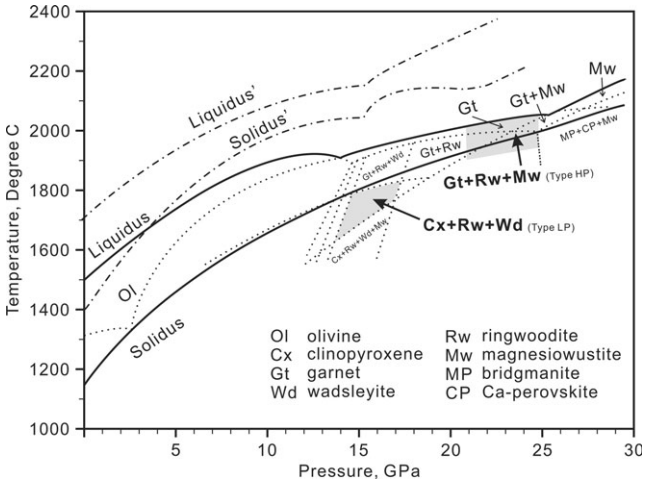

Fig. 7. A simplified liquidus phase diagram of Allende meteorite after Agee et al. (1995) and the solidus and liquidus (dot-dash lines) for KLB-1 peridotite from Zhang and Herzberg (1994). The garnet plus magnesiowüstite and ringwoodite are the crystallization assemblage between 20 and 25 GPa. The Type LP matrix assemblage can occur at subsolidus temperature from 14 to 17 GPa. The highest temperature of this field is close to the solidus at 15 GPa.

crystallization of subsolidus phases. The consistent round sulfide droplets throughout the Type LP matrix are also evidence for a fast quench. However, the cooling rate of Type LP matrix was not rapid enough to quench to a glass.

Based on the Allende phase diagram, clinoenstatite can occur at pressures of 14–17 GPa under high temperature close to the solidus (Fig. 7). This pressure range is compatible with the stability field of the wadsleyite and ringwoodite. Nevertheless, the slight compositional difference between the Type LP matrix and Allende may influence the pressure estimation. Compared with Allende and KLB-1, the Type LP melt matrix is slightly depleted in aluminum and calcium, but much more enriched in sodium (Table 3). The relatively low magnesium concentration of the silicate in Type LP matrix is affected by the Fe distribution in silicate, oxide, sulfide, and metal. Previous high-pressure experiments suggest pure Na-Mg pyroxene ($NaMg_{0.5}Si_{0.5}Si_2O_6$) can survive through high pressure before the transformation to sodium-rich majorite (Dymshits et al. 2010). The Clapeyron slope for the Na-enstatite to Na-majorite transition is positive. At temperatures near the solidus, the boundary pressure can be as high as 18 GPa. We are not suggesting that the crystallization pressure of a phase is exactly the same as its stability field in solid state. However, the experimental data indicate that the sodium-bearing clinopyroxene (Table 2) can be a high-pressure phase. The assemblage of clinopyroxene and wadsleyite in

Type LP melt thus are consistent with static high-pressure experiments and a crystallization pressure of ~15 GPa.

In summary, we suggest the shock pressure of NWA 757 is indicated by the Type HP melt matrix at 20–25 GPa. If the shock pressure was significantly higher than this, we would expect the crystallization of bridgmanite and/or akimotoite in fast-quenched melt veins and postspinel transformation in olivine, like those seen in L chondrite Tenham, Acfer 040, and shergottites DaG 735 and Tissint (Sharp et al. 1997; Tomioka and Fujino 1997; Miyahara et al. 2011a, 2011b; Tschauner et al. 2014; Walton et al. 2014). The origin of the Type LP matrix is discussed in the following section.

Formation of Two Crystallization Assemblages

In the previous sections we showed that the two types of melt are distinct in mineralogy, microtexture, and crystallization pressure. The origin of the two types of quenched melt might be explained by (1) two vein-forming events in a single shock, (2) differences in chemical compositions, or (3) two shock events with different shock pressures.

Type HP matrix contains coarse-grained liquidus-phase garnet with interstitial ringwoodite and magnetite. In contrast, Type LP matrix consists of fine-grained subhedral clinopyroxene and wadsleyite. A simple interpretation of the difference in crystallization pressure (20–25 GPa versus 15 GPa) is that Type LP matrix quenched at lower pressure during decompression. For example, in the S6 L6 chondrite Tenham, the crystallization assemblage changes at the melt vein edge through the vein interior (Tomioka and Fujino 1997; Xie et al. 2006a). In Tenham, because the shock melt cools by conducting heat into the colder host rock, the edge of the melt vein quenches faster than the vein interior and crystallizes the assemblage of fine-grained akimotoite and bridgmanite. The vein interior then experiences a longer quench time and later crystallization. The pressure decreases during quench resulting in coarse-grained majorite in the vein interior. However, in NWA 757 the high-pressure Type HP matrix does not exclusively occur along the vein margins and/or thin veins. On the contrary, Type HP matrix crystallizes coarse-grained garnet in thick melt pockets and vein centers. This texture cannot be explained by a single melt-vein quench from high to low pressure. Different melt-formation mechanisms and timing must be considered.

Shock vein formation involves localized pore collapse, comminution, and friction on fractures and grain boundaries (Spray 1995, 1998; Langenhorst and Poirier 2000; Sharp and DeCarli 2006). The collapse of pores behind the shock front significantly increases the bulk and localized shock temperature as well as the postshock temperature (Sharp and DeCarli 2006). Friction on fractures and grain boundaries during compression–decompression generates partially to fully melted pseudotachylitic zones. In principle, shearing can occur during decompression when the confining pressure decreases more rapidly than the deviatoric component of the stress tensor (Langenhorst and Poirier 2000). Langenhorst et al. (2002) performed a shock-shearing experiment on a single crystal of olivine. The frictional melting was inferred to occur as the rarefaction wave traversed during decompression. Evidence of frictional melting by shock compression–decompression is observed in terrestrial impact structures (Spray 1998). These previous studies suggest that the shear veining can occur throughout the shock from compression to release. In realistic planetary impacts, the localized shock pressure history is dependent on the geometry of the colliding bodies as well as the small-scale heterogeneities in shock impedance (Stöffler et al. 1991; Melosh et al. 1992). If multiple shear veining events occur during shock, the crystallization assemblages would therefore reflect varying shock pressure versus time rather than an ideal equilibrium shock pressure before decompression. Specifically for NWA 757, pores collapse and shear and friction lead to melt veins and pockets during compression. This shock melt quenches at the peak shock pressure to crystallize garnet plus Fe-Mg oxides, but may leave residual silicate melt plus sulfide melt droplets. If the solidification of the melt matrix proceeds without local disturbance, the spherical shape of sulfide droplets would be preserved (Figs. 3b and 8a). Locally, secondary shear leads to new melt veins and deforms the partially solidified Type HP melt veins, as well as smears the sulfide droplets inside the veins (Fig. 8b). The new melt vein subsequently quenches at slightly lower pressure, likely resulting from decompression, and crystallizes the pyroxene-predominate matrix. Significantly, this scenario does not necessarily require the higher pressure matrix to quench faster than the lower pressure matrix. The partial crystallization of Type HP melt can occur before the formation of Type LP melt. The secondary veining event preserves a record of lower shock pressure conditions.

The composition of silicate in the two types of melt is different primarily in sodium content. Although sodium can increase the pressure stability of pyroxene (Dymshits et al. 2010), the crystallization pressures of Type HP matrix of 20–25 GPa is still well above the range for sodic pyroxenes in Type LP matrix. The

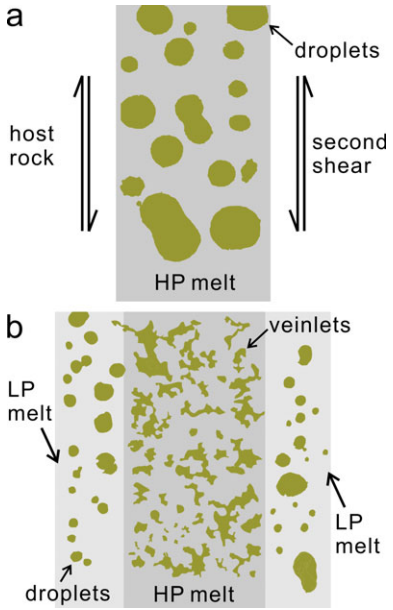

Fig. 8. The two-stage formation of Type HP and Type LP melt matrices corresponding to Fig 3f. a) The early melt vein crystallizes a garnet-bearing Type HP melt matrix with spherical droplets of immiscible sulfide melt before the second shear event. b) Secondary shearing in this area creates new shock melt around the early melt and smears the sulfide droplets into veinlets in the Type HP melt. The new shock melt vein subsequently crystallizes the clinopyroxene-bearing Type LP matrix. The solidification of the LP melt occurs in a relatively low shear stress environment and preserves the round droplets of immiscible sulfide.

higher iron content in Type LP matrix might make a small difference because ferrous iron is slightly preferred in garnet compared to clinoenstatite (Irifune and Isshiki 1998). However, this is a minor effect when magnesiowüstite and ringwoodite/wadsleyite coexist in the assemblage. Therefore, the small compositional variation between Type HP and Type LP matrix cannot account for their distinct mineral assemblages.

From our characterization, we cannot rule out the possibility that multiple shock events formed the two melts. Chen and Xie (2008) reported coexisting melt veins of different mineralogy and texture in the Sixiangkou L6 chondrite. They used cross-cutting relations and sharp boundaries between the shock veins to conclude that a second shock event was needed to explain the two veins. The authors also discussed the possibility of successive shear melting in one shock event, but ruled it out based on the sharp edges and consistent crosscutting relationship between the early and late vein. In our sample, the diffuse boundary (Fig. 3e) between the two matrices suggests that the Type LP veining event occurred while the Type HP veins were still partially molten. In local areas, the boundaries between the two veins can be sharp and well defined by variations in metal sulfide textures (Fig. 3f). However, metal-sulfide textures vary depending more on the initial sulfide abundance in the melt and shearing stress during shock-vein quench. Spherical sulfide droplets are preserved by fast quench of melt under relatively low shear stresses. FIB-TEM does not indicate a sharp transition between crystallized silicates in these areas. Moreover, the Type LP matrix occurring together with Type HP matrix (Fig. 3f) could be the result of the LP veining event occurring over the pre-existing HP vein. Our sample also lacks a consistent crosscutting relationship between the two matrices (Fig. 3e). The textures in our sample are ambiguous, but they are not clearly indicative of two shock events.

Impact on LL Chondrite Parent Body

In order to constrain the impact history of the LL chondrite parent body, information from shock metamorphism and impact age dating of meteorite samples are needed. Previous studies of shock metamorphism in L chondrites help reveal the shock conditions on the L chondrite parent body. Particularly, the shock melt crystallization assemblage can constrain both the shock pressure and the pulse duration (Sharp and DeCarli 2006). The Type HP matrix of majoritic garnet plus magnesiowüstite-magnetite suggests a crystallization pressure up to 25 GPa. The same crystallization assemblage has been reported in L6 chondrites of shock stage S6, such as Sixiangkou and Tenham (Chen et al. 1996; Xie et al. 2006a). Although higher pressure phases, including bridgmanite, in Acfer 040 and Tenham indicate excessive shock pressure in some S6 L chondrites (Sharp et al. 1997; Tomioka and Fujino 1997; Tschauner et al. 2014), NWA 757 likely experienced a shock pressure similar to most S6 L chondrites. Another important factor to constrain the impact conditions is the shock-pulse duration. A lower bound of shock-pulse duration is set by the quench time of a melt vein that contains a consistent high-pressure assemblage. The quench time is dependent on the thermal conductivity, specific heat, and density of the material as well as the temperature gradient around the hot spot (Sharp et al. 2015). Qualitatively, a melt pocket with other adjacent melt veins has a smaller temperature gradient and therefore quenches slower than the same pocket surrounded by cooler host rock, given the same initial melt temperature. Shaw and Walton (2013) modeled the temperature history of shock melt in several meteorites. Their model suggests that the melt veins with ~1 mm thickness require a time scale of about 1 second to quench to the high-pressure solidus. In NWA 757, connected melt veins and pockets

thicker than 1 mm are common (Fig 1a). The quench time of the veins are therefore on the order of 1 second. Taking 1 second as the lower bound of the shock pulse, this time scale is close to the shock pulse of L chondrites estimated from heat flow modeling (DeCarli et al. 2012), crystallization kinetics (Ohtani et al. 2004), and diffusion profiles (Beck et al. 2005). The shock pressure and pulse duration reflect the velocity and size of the impact (Melosh 1989). Hydrocode simulations and flat impact approximations both suggest that the typical highly shocked L chondrites result from the impact of a projectile-target larger than 10 km (Ohtani et al. 2004; DeCarli et al. 2012). Therefore, similarly NWA 757 was probably shocked by an impact between bodies larger than 10 km diameter.

The impact ages of meteorites provide important constraints on the impact histories of parent bodies. $^{39}Ar/^{40}Ar$ dating of many L chondrite melt breccias show several impact events with a major spike at ~470 Ma suggesting a catastrophic impact (Turner 1969; McConville et al. 1988; Bogard 1995; Korochantseva et al. 2007; Weirich et al. 2012; Swindle et al. 2014). Although not all L chondrites have been age dated, the shock metamorphic features of L chondrites, combined with collisional models and age dating results, are consistent with a recent large impact event on the L parent body. Previous studies of LL chondrites do not suggest a single catastrophic collision. The Ar-Ar ages of LL chondrites show a spike between 4175 and 4340 Ma, suggesting a distinct early impact history on the parent body (Swindle et al. 2014). Some LL chondrites also have impact ages less than 1200 Ma. However, the data are not sufficient to extract the ages of a single or several events (Swindle et al. 2014). In contrast to highly shocked L chondrites, highly shocked S5-6 LL chondrites have been missing from meteorite collections (Stöffler et al. 1991). Kimura et al. (2001) reported jadeite coexisting with olivine and orthopyroxene in a shock melt from LL chondrite Y-8410 and conclude a lower pressure and shorter duration shock on the LL chondrite parent body than those of L chondrites. The distinct difference between the impact age and degree of shock metamorphism between L and LL chondrites can result from either distinct impact histories on the parent bodies or stochastic sampling of shocked materials. The shock features reported here in NWA 757 suggest that at least a portion of LL chondrite parent body was intensely shocked in a relatively large impact similar to those on the L chondrite parent body. However, the resulting highly shocked material is rarely captured by the Earth. The hypothesis of stochastic rather than continuous sampling of LL chondrites is consistent with the cosmic ray exposure age. Marti and Graf (1992) summarized the cosmic ray exposure age distribution of 44 LL chondrites. A well-concentrated peak at 15 Ma suggests a major meteoroid or major meteoroids that brought the LL material to the Earth. These meteoroids are likely from the weakly shocked portion of the parent body. Although the relatively high proportion of shocked samples among L chondrites is probably biased by a single impact event, NWA 757 suggests that a similarly intense impact also occurred on the LL parent body. This result implies that large impacts may have been common among chondrite asteroids. Further work on impact age(s) and cosmic ray exposure age(s) are needed to better understand the space history of NWA 757.

The recent Chelyabinsk airburst event provided abundant fresh LL material. Ozawa et al. (2014) report jadeite crystallized from feldspar melt in one Chelyabinsk meteorite sample. They conclude a moderate pressure of shock (3–12 GPa) and low-velocity impact on the Chelyabinsk asteroid. Rb-Sr, Sm-Nd, and Ar-Ar ages of the Chelyabinsk meteorites suggests a complicated impact history of the parent body (Lindsay et al. 2015; Righter et al. 2015). The argon ages are diverse from 32 Ma to ~2800 Ma. The diversity of impact age as well as less intense shock metamorphism is similar to the other LL chondrites, which represent weakly shocked source meteoroids. Further study of LL material is needed to better understand the history of its parent body.

CONCLUSION

NWA 757 is a unique highly shocked LL chondrite that includes high-pressure minerals ringwoodite, tuite, and lingunite formed by solid-state transformation. Quenched shock melt resulted in two shock-melt assemblages (1) majoritic garnet, ringwoodite plus magnetite-magnesiowüstite and (2) clinopyroxene plus wadsleyite. The former assemblage indicates veining and melt crystallization at shock pressures of 20–25 GPa while the latter represents successive shear veining and quench at ~15 GPa. The presence of lower pressure melt matrix suggests that secondary shearing and veining can occur in one shock event. The high-pressure minerals in this LL chondrite are more similar to those in highly shocked L chondrites than those in other LL chondrites. The similarity between shock-vein mineralogy and melt-vein thickness in NWA 757 and those of highly shocked L chondrites suggests that the impact event that shocked NWA 757 is likely comparable to the catastrophic impact events on the L parent body. It appears that NWA 757 represents a highly shocked portion of the LL chondrite parent body.

Acknowledgments—We thank Dr. Oliver Tschauner, Dr. Adrian Brearley, and the anonymous reviewer for the constructive comments to this paper. NASA Cosmochemistry Grants NNG06GF09G and NN09AG41G supported this research. We thank B.S. students Riley Trickey and Brandon Kent for their contributions to this work and the NASA Arizona Space Grant Consortium for supporting them. We thank A. Bischoff and the Institut für Planetologie/ICEM for supplying the NWA 757 sample. We thank Dr. Kurt Leinenweber for the help with refining the X-ray diffraction patterns. We gratefully acknowledge the use of facilities within the LeRoy Eyring Center for Solid State Science at Arizona State University. Synchrotron X-ray diffraction was performed at GeoSoilEnviroCARS (Sector 13), Advanced Photon Source (APS), Argonne National Laboratory. GeoSoilEnviroCARS is supported by the National Science Foundation–Earth Sciences (EAR-1128799) and Department of Energy–GeoSciences (DE-FG02-94ER 14466). This research used resources of the Advanced Photon Source, a U.S. Department of Energy (DOE) Office of Science User Facility operated for the DOE Office of Science by Argonne National Laboratory under Contract No. DE-AC02-06CH11357.

Editorial Handling—Dr. Adrian Brearley

REFERENCES

Agee C. B., Li J., Shannon M. C., and Circone S. 1995. Pressure-temperature phase diagram for the Allende meteorite. *Journal of Geophysical Research: Solid Earth* 100:17,725–17,740.

Asahara Y., Kubo T., and Kondo T. 2004. Phase relations of a carbonaceous chondrite at lower mantle conditions. *Physics of the Earth and Planetary Interiors* 143–144:421–432.

Beck P., Gillet P., El Goresy A., and Mostefaoui S. 2005. Timescales of shock processes in chondritic and Martian meteorites. *Nature* 435:1071–1074.

Bischoff A. 2002. Discovery of purple-blue ringwoodite within shock veins of an LL6 ordinary chondrite from Northwest Africa (abstract #1264). 33rd Lunar and Planetary Science Conference. CD-ROM.

Bogard D. 1995. Impact ages of meteorites: A synthesis. *Meteoritics* 30:244–268.

Chen M. and Xie X. 2008. Two distinct assemblages of high-pressure liquidus phases in shock veins of the Sixiangkou meteorite. *Meteoritics & Planetary Science* 43:823–828.

Chen M., Sharp T. G., Goresy A. E., Wopenka B., and Xie X. 1996. The majorite-pyrope + magnesiowustite assemblage: Constraints on the history of shock veins in chondrites. *Science* 271:1570–1573.

Chen M., Goresy A. E., Gillet P., and Mao H. 2004. Ringwoodite lamellae in olivine: Clues to olivine-ringwoodite phase transition mechanisms in shocked meteorites and subducting slabs. *Proceedings of the National Academy of Sciences* 101:15,033–15,037.

DeCarli P. S., Xie Z., Trickey R., Hu J., Weaver C., and Sharp T. 2012. High-pressure minerals in RC 106 provide evidence for a very large impact (abstract #2877). 43rd Lunar and Planetary Science Conference. CD-ROM.

Dymshits A. M., Bobrov A. V., Litasov K. D., Shatskiy A. F., Ohtani E., and Litvin Y. A. 2010. Experimental study of the pyroxene-garnet phase transition in the $Na_2MgSi_5O_{12}$ system at pressures of 13–20 GPa: First synthesis of sodium majorite. *Doklady Earth Sciences* 434:1263–1266.

Ferroir T., Beck P., Van de Moortèle B., Bohn M., Reynard B., Simionovici A., El Goresy A., and Gillet P. 2008. Akimotoite in the Tenham meteorite: Crystal chemistry and high-pressure transformation mechanisms. *Earth and Planetary Science Letters* 275:26–31.

Grew E. S., Locock A. J., Mills S. J., Galuskina I. O., Galuskin E. V., and Hålenius U. 2013. Nomenclature of the garnet supergroup. *American Mineralogist* 98: 785–811.

Hirose K., Fei Y., Ma Y., and Mao H.-K. 1999. The fate of subducted basaltic crust in the Earth's lower mantle. *Nature* 397:53–56.

Hogrefe A., Rubie D. C., Sharp T. G., and Seifert F. 1994. Metastability of enstatite in deep subducting lithosphere. *Nature* 372:351–353.

Irifune T., and Isshiki M. 1998. Iron partitioning in a pyrolite mantle and the nature of the 410-km seismic discontinuity. *Nature* 392:702–705.

Kerschhofer L., Dupas C., Liu M., Sharp T. G., Durham W. B., and Rubie D. C. 1998. Polymorphic transformations between olivine, wadsleyite and ringwoodite; mechanisms of intracrystalline nucleation and the role of elastic strain. *Mineralogical Magazine* 62:617–638.

Kimura M., Suzuki A., Kondo T., Ohtani E., and El Goresy A. 2000. Natural occurrence of high-pressure phases, jadeite, hollandite, wadsleyite, and majorite-pyrope garnet, in an H chondrite, Yamato 75100. *Meteoritics & Planetary Science Supplement* 35:A87.

Kimura M., Suzuki A., Ohtani E., and El Goresy A. 2001. Raman petrography of high-pressure minerals in H, L, LL and E-chondrites. *Meteoritics and Planetary Science Supplement* 36:A99.

Kimura M., Chen M., Yoshida Y., El Goresy A., and Ohtani E. 2003. Back-transformation of high-pressure phases in a shock melt vein of an H-chondrite during atmospheric passage: Implications for the survival of high-pressure phases after decompression. *Earth and Planetary Science Letters* 217:141–150.

Korochantseva E. V., Trieloff M., Lorenz C. A., Buykin A. I., Ivanova M. A., Schwarz W. H., Hopp J., and Jessberger E. K. 2007. L-chondrite asteroid breakup tied to Ordovician meteorite shower by multiple isochron ^{40}Ar-^{39}Ar dating. *Meteoritics & Planetary Science* 42:113–130.

Langenhorst F. and Poirier J.-P. 2000. Anatomy of black veins in Zagami: Clues to the formation of high-pressure phases. *Earth and Planetary Science Letters* 184:37–55.

Langenhorst F., Poirier J.-P., Deutsch A., and Hornemann U. 2002. Experimental approach to generate shock veins in single crystal olivine by shear melting. *Meteoritics & Planetary Science* 37:1541–1553.

Larsen A. and Von Dreele R. 1994. *GSAS, general structure analysis system*. LANSCE, MS-H805. Los Alamos, New Mexico: Los Alamos National Laboratory.

Lindsay F., Herzog G., Park J., Turrin B., Delaney J., and Swisher C. 2015. Chelyabinsk Ar-Ar ages—A young heterogeneous LL5 chondrite (abstract #2226). 46th Lunar and Planetary Science Conference. CD-ROM.

Marti K. and Graf T. 1992. Cosmic-ray exposure history of ordinary chondrites. *Annual Review of Earth and Planetary Sciences* 20:221–243.

McConville P., Kelley S., and Turner G. 1988. Laser probe ^{40}Ar-^{39}Ar studies of the Peace River shocked L6 chondrite. *Geochimica et Cosmochimica Acta* 52:2487–2499.

Melosh H. J. 1989. *Impact cratering: A geologic process*. Oxford: Oxford University Press. 253 p.

Melosh H. J., Ryan E. V., and Asphaug E. 1992. Dynamic fragmentation in impacts: Hydrocode simulation of laboratory impacts. *Journal of Geophysical Research: Planets* 97:14,735–14,759.

Miyahara M., El Goresy A., Ohtani E., Kimura M., Ozawa S., Nagase T., and Nishijima M. 2009. Fractional crystallization of olivine melt inclusion in shock-induced chondritic melt vein. *Physics of the Earth and Planetary Interiors* 177:116–121.

Miyahara M., Ohtani E., Kimura M., El Goresy A., Ozawa S., Nagase T., Nishijima M., and Hiraga K. 2010. Coherent and subsequent incoherent ringwoodite growth in olivine of shocked L6 chondrites. *Earth and Planetary Science Letters* 295:321–327.

Miyahara M., Ohtani E., Kimura M., Ozawa S., Nagase T., Nishijima M., and Hiraga K. 2011a. Evidence for multiple dynamic events and subsequent decompression stage recorded in a shock vein. *Earth and Planetary Science Letters* 307:361–368.

Miyahara M., Ohtani E., Ozawa S., Kimura M., El Goresy A., Sakai T., Nagase T., Hiraga K., Hirao N., and Ohishi Y. 2011b. Natural dissociation of olivine to (Mg, Fe)SiO3 perovskite and magnesiowüstite in a shocked Martian meteorite. *Proceedings of the National Academy of Sciences* 108:5999–6003.

Ohtani E., Kimura Y., Kimura M., Takata T., Kondo T., and Kubo T. 2004. Formation of high-pressure minerals in shocked L6 chondrite Yamato 791384: Constraints on shock conditions and parent body size. *Earth and Planetary Science Letters* 227:505–515.

Ozawa S., Ohtani E., Miyahara M., Suzuki A., Kimura M., and Ito Y. 2009. Transformation textures, mechanisms of formation of high-pressure minerals in shock melt veins of L6 chondrites, and pressure-temperature conditions of the shock events. *Meteoritics & Planetary Science* 44:1771–1786.

Ozawa S., Miyahara M., Ohtani E., Koroleva O. N., Ito Y., Litasov K. D., and Pokhilenko N. P. 2014. Jadeite in Chelyabinsk meteorite and the nature of an impact event on its parent body. *Scientific Reports* 4:1–5.

Righter K., Abell P., Agresti D., Berger E., Burton A., Delaney J., Fries M., Gibson E., Harrington R., and Herzog G. 2015. Mineralogy, petrology, chronology, and exposure history of the Chelyabinsk meteorite and parent body (abstract #2686). 46th Lunar and Planetary Science Conference. CD-ROM.

Sharp T. G. and DeCarli P. S. 2006. Shock effects in meteorites. In *Meteorites and the early solar system II*, edited by Lauretta D. S. and McSween H. Y. Tucson, Arizona: University of Arizona Press. pp. 653–677.

Sharp T. G., Lingemann C. M., Dupas C., and Stöffler D. 1997. Natural occurrence of $MgSiO_3$-ilmenite and evidence for $MgSiO_3$-perovskite in a shocked l chondrite. *Science* 277:352–355.

Sharp T. G., Xie Z., de Carli P. S., and Hu J. 2015. A large shock vein in L chondrite Roosevelt County 106: Evidence for a long-duration shock pulse on the L chondrite parent body. *Meteoritics & Planetary Science* 50:1941–1953.

Shaw C. S. J. and Walton E. 2013. Thermal modeling of shock melts in Martian meteorites: Implications for preserving Martian atmospheric signatures and crystallization of high-pressure minerals from shock melts. *Meteoritics & Planetary Science* 48:758–770.

Spray J. G. 1995. Pseudotachylyte controversy: Fact or friction? *Geology* 23:1119–1122.

Spray J. G. 1998. Localized shock- and friction-induced melting in response to hypervelocity impact. *Geological Society, London, Special Publications* 140:195–204.

Stöffler D., Keil K., and Scott E. R. D. 1991. Shock metamorphism of ordinary chondrites. *Geochimica et Cosmochimica Acta* 55:3845–3867.

Swindle T. D., Kring D. A., and Weirich J. R. 2014. ^{40}Ar/^{39}Ar ages of impacts involving ordinary chondrite meteorites. *Geological Society, London, Special Publications* 378:333–347.

Toby B. H. 2001. EXPGUI, a graphical user interface for GSAS. *Journal of Applied Crystallography* 34:210–213.

Tomioka N. and Fujino K. 1997. Natural (Mg, Fe)SiO_3-ilmenite and -perovskite in the Tenham meteorite. *Science* 277:1084–1086.

Tschauner O., Ma C., Beckett J. R., Prescher C., Prakapenka V. B., and Rossman G. R. 2014. Discovery of bridgmanite, the most abundant mineral in Earth, in a shocked meteorite. *Science* 346:1100–1102.

Turner G. 1969. Thermal histories of meteorites by the ^{39}Ar-^{40}Ar method. In *Meteorite research*, edited by Millman P. M. Amsterdam, the Netherlands: Springer. pp. 407–417.

Walton E. L., Sharp T. G., Hu J., and Filiberto J. 2014. Heterogeneous mineral assemblages in Martian meteorite Tissint as a result of a recent small impact event on Mars. *Geochimica et Cosmochimica Acta* 140:334–348.

Weirich J. R., Swindle T. D., and Isachsen C. E. 2012. ^{40}Ar-^{39}Ar age of Northwest Africa 091: More evidence for a link between L chondrites and fossil meteorites. *Meteoritics & Planetary Science* 47:1324–1335.

Xie Z., Sharp T. G., and DeCarli P. S. 2006a. High-pressure phases in a shock-induced melt vein of the Tenham L6 chondrite: Constraints on shock pressure and duration. *Geochimica et Cosmochimica Acta* 70:504–515.

Xie Z., Sharp T. G., and DeCarli P. S. 2006b. Estimating shock pressures based on high-pressure minerals in shock-induced melt veins of L chondrites. *Meteoritics & Planetary Science* 41:1883–1898.

Xie X., Zhai S., Chen M., and Yang H. 2013. Tuite, γ-$Ca_3(PO_4)_2$, formed by chlorapatite decomposition in a shock vein of the Suizhou L6 chondrite. *Meteoritics & Planetary Science* 48:1515–1523.

Zhang J. and Herzberg C. 1994. Melting experiments on anhydrous peridotite KLB-1 from 5.0 to 22.5 GPa. *Journal of Geophysical Research: Solid Earth* 99:17729–17742.

SUPPORTING INFORMATION

Additional supporting information may be found in the online version of this article:

Fig. S1. The petrology and shock metamorphism in the host rock of NWA 757. a) Cross-polarized light (XPL) image of an olivine clast with undulatory extinction in the center of the view. b) Mosaicism extinction in an olivine clast (center) under XPL. c) Plane-polarized light (PPL) image of clear maskelynite (msk) and crystalline plagioclase (pl). The opaque minerals are troilite. d) The XPL image of (c). The maskelynite is isotropic and the plagioclase shows first-order gray interference colors. e) PPL image of fine-grained unequilibrated plagioclase and large olivine clasts. f) Reflected light image of (e). The plagioclase (dark contrast) has chromite inclusions. The insert is an enlargement of the area in the white box. The bright patches in the olivine clasts are remnant carbon coat.

Fig. S2. Olivine partially transformed to ringwoodite from the same clast in Fig. 3a. The upper figure is a SEM BSE image of the whole clast and the lower figure is the corresponding Raman spectra. The red, green, and blue spectra are taken from the circle spots of the same colors, respectively. All the three spectra show ringwoodite 231 cm^{-1} peaks and strong fluorescent background. Only the red spectrum shows the ringwoodite 798 cm^{-1} peak, whereas the other two include the olivine 825 cm^{-1} peak. The olivine spectrum in Fig. 2 is taken from the white spot.